energies

MDPI

Article

Methodology for Modeling Multiple Non-Homogeneous Thermal Zones Using Lumped Parameters Technique and Graph Theory

Frank Florez [1,*], Jesús Alejandro Alzate-Grisales [1], Pedro Fernández de Córdoba [2] and John Alexander Taborda-Giraldo [3]

[1] Faculty of Engineering, Universidad Autónoma de Manizales, Manizales 170003, Colombia
[2] Instituto Universitario de Matemática Pura y Aplicada, Universitat Politècnica de València, Camino de Vera s/n, 46022 Valencia, Spain
[3] Universidad del Magdalena, Santa Marta, Colombia
* Correspondence: frank.florezm@autonoma.edu.co

Abstract: Asymmetric thermal zones or even non-rectangular structures are common in residential buildings. These types of structures are not easy to model with specialized programs, and it is difficult to know the heat flows and the relationships between the different variables. This paper presents a methodology for modeling structures with multiple thermal zones using the graph theory arrangement. The methodology allows for generating a mathematical model using all the walls of each thermal zone. The modeling method uses the lumped parameter technique with a structure of two resistors and two capacitors for each thermal zone. The walls and internal surfaces of each zone define the thermal resistances, and the elements for the network structure are created by reducing resistances. The structure selected as a case study is similar to a residential apartment, which demonstrates the possibility of modeling complex and non-traditional structures. The accuracy of the generated mathematical model is verified by comparison with experimental data recorded in a scaled-down model. The reduced model is constructed using a 1:10 ratio with a real apartment. The proposed methodology is used to generate a graph arrangement adjusted to the case study, using the surfaces to build the mathematical model. The experimental data allowed to adjust the simulation results with errors in the range of 1.88% to 6.63% for different thermal zones. This methodology can be used to model different apartments, offices, or non-asymmetric structures and to analyze individual levels in buildings.

Keywords: mathematical model; graph theory; buildings; lumped parameters; thermal zones; scale-reduced model; contact matrix; experimental test

check for updates

Citation: Florez, F.; Alzate-Grisales, J.A.; Fernández de Córdoba, P.; Taborda-Giraldo, J.A. Methodology for Modeling Multiple Non-Homogeneous Thermal Zones Using Lumped Parameters Technique and Graph Theory. *Energies* **2023**, *16*, 2693. https://doi.org/10.3390/en16062693

Academic Editors: Adelio Mendes, João M. P. Q. Delgado and Ana Sofia Guimarães

Received: 28 January 2023
Revised: 23 February 2023
Accepted: 5 March 2023
Published: 14 March 2023

Copyright: © 2023 by the authors. Licensee MDPI, Basel, Switzerland. This article is an open access article distributed under the terms and conditions of the Creative Commons Attribution (CC BY) license (https://creativecommons.org/licenses/by/4.0/).

1. Introduction

The development of the Sustainability Goals (SDGs) formulated by the United Nations (UN) encourages the reduction of energy consumption in cities and urban regions [1]. To achieve this goal, it is necessary to study different aspects of buildings, such as thermal comfort and energy uses [2,3].

Building energy is related to the consumption of individual apartments or spaces. It is estimated that one third of the world's energy consumption is accounted for by HVAC systems, and about 20% of the energy is devoted to residential buildings alone. For all these reasons, building modeling is a booming area of study [4–6], generating new strategies for multi-zone analysis such as for apartments and individual dwellings, as well as being related to complex concepts such as thermal comfort, especially its subjective character.

Thermal comfort is the most energy-consuming aspect in homes and offices. This comfort aspect refers to the mental and physical state in which an individual feels pleasant

with the ambient temperature; it is a subject of human physiology and engineering concerned with the recommendation of temperature and humidity levels and other factors such as air velocity, clothing insulation, and metabolic rate, to achieve thermal comfort. It is also sometimes referred to as thermal acceptability. Thermal comfort can be quantified using the PMV (predicted mean vote) or PPD (predicted percentage of dissatisfied) indices [7]. Different studies have shown that suboptimal temperature conditions can lead to stress, which has an impact on the individual's health, behavior, and productivity in a work environment [8–10]. Considering that, in urban settings, people spend more than 80% of their time indoors [11], one can imagine the energy expenditure associated with maintaining thermal comfort conditions for people inside buildings and dwellings, especially in countries with extreme temperature changes between seasons. In addition, rising temperatures due to climate change have caused the maintenance of indoor thermal comfort to be the subject of extensive studies, seeking to maintain a healthy and productive environment for inhabitants [12,13].

To mitigate the effects of climate change, concepts such as smart cities have been developed in recent decades [14–16]. These cities seek to reduce the environmental impact of each inhabitant and their energy consumption. In many cases, excessive energy use is energy waste, and is related to the overuse of heating, ventilation, and air conditioning (HVAC) systems, which can consume up to 40% of the energy produced worldwide in a year [17–19]. Therefore, it is necessary to understand, design, and apply solutions to maintain thermal comfort conditions and reduce energy consumption.

Currently, there are multiple solutions to guarantee thermal comfort [20–22]. Some of these solutions are cool roofs, green roofs, and solar roofs. These strategies have been growing hand-in-hand with technological tools such as artificial intelligence (AI). A review of the literature shows that AI-based thermal comfort models have been developed using various methods, including rule-based systems, decision trees, artificial neural networks, and support vector machines. These models have been applied to a variety of data sources, including building energy consumption data, indoor temperature, humidity data, and survey data [17,18,23–26].

In a related study, Gao et al. [27] used reinforcement learning to predict optimal thermal comfort control, minimizing both HVAC energy consumption and occupant thermal comfort perception, in a two-stage architecture that first predicts occupant thermal comfort, and then predicts the control policy. In similar research work, Chaudhuri et al. [28] implemented feed-forward neural networks to achieve the optimal operating state in which thermal comfort is achieved with the minimum energy consumption; such a system had a potential energy savings of up to 36.5%. Moon et al. [29] constructed two independent artificial neural networks that predict the optimal start time of the cooling system and the total energy consumption to recover the set temperature after a sudden change; both predictions are incorporated into a temperature control loop that reduces energy consumption. Similarly, Yu et al. [30] used an improved multi-objective genetic algorithm to optimize a neural network to predict the energy consumption and indoor thermal comfort status of residential buildings; the results show that this model is an effective tool for building optimization design.

A different approach has been to build mathematical models that can accurately describe the heat transfer behavior in closed environments with single or multiple connected rooms, given the complex nature of the system with multiple heat sources and various forms of interaction, such as convection or radiation, the construction of these models is a rather difficult task [31]. Wang et al. [32] studied the total heat transfer coefficients of floor surfaces with radiant heating systems, aiming to improve the design process of these systems and accurately adjust the heating capacities in each situation. In a different study, Hu et al. [33] created a mathematical model for air distribution in large-space buildings, where, given the distance from floor to ceiling, it is often necessary to implement stratified air conditioning systems; the model aims to compare different layouts in terms of energy consumption and cooling capacities. On a similar topic, Aghamolaei et al. [34] analyzed

outdoor thermal comfort in highly populated urban environments, aiming to determine the impact of densely built-up areas and their interaction with solar radiation and wind, versus natural areas.

This work focuses on the development of a methodology for the construction of mathematical models of non-homogeneous thermal zones based on graph theory and the lumped parameters technique. The proposed algorithm can generate a suitable model for a closed space given the thermal zones and their interaction. In addition, a program is used to tune the coefficients of the mathematical model, based on the pattern search algorithm. This program is developed in MATLAB software and requires the experimental data to provide the appropriate values for each zone. The difference between the simulated and experimental internal temperature is used as an objective function, searching for the coefficients that reduce this difference during a single cycle. Finally, the resulting models are fitted and validated against an apartment-scale construction over multiple charge/discharge cycles. In this paper we intend to demonstrate that this type of mathematical model can also be applied to much more complex structures, allowing multi-zone analysis by means of graph theory settings. In this paper, we focus on the application of the methodology to structures with complex geometries, similar to real residential apartments. To do so, we take advantage of the experience and validations performed in previous works [35–39].

2. Material and Methods

2.1. Mathematical Theory

In real applications, uniformity of thermal zones is not common. In many cases, especially in older buildings, rooms can have a different number of walls in the same apartment. For this reason, mathematical models must consider the possibility of analyzing heterogeneous spaces with different areas and surfaces. Figure 1 illustrates the possibility of finding m thermal zones with n surfaces for each thermal zone. In many cases, some surfaces link two zones, and in other cases, the surface delimits the zone and the environmental conditions [40,41].

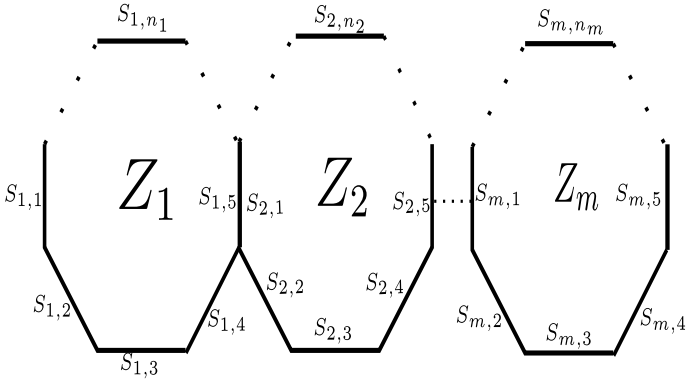


Figure 1. Multiple heterogeneous thermal zones.

Each surface can be named using the nomenclature $S_{i,j}$ where i corresponds to the thermal zone number, and the subscript j shows the surface number of the corresponding zone. For example, the surface $S_{2,3}$ represents the third surface of the second thermal zone. This notation allows using a different surface number for each thermal zone, taking $n_1, n_2, \ldots, n_m$ as the surfaces for the zones $Z_1, Z_2, \ldots, Z_m$. The notation for multiple heterogeneous thermal zones can work with graph theory. In this application, it is possible to take the different zones as nodes, and the contact surfaces between zones for edges; Figure 2 illustrates the graph scheme for m thermal zones [42,43].

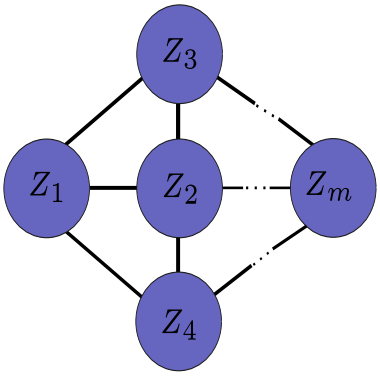


Figure 2. Graph scheme for thermal zones.

According to the literature, a graph G consists of two elements. The first element is a finite set containing V vertices [44,45]. The Set V can be expressed as $V = x_0, x_1, \ldots, x_k$, taking k as the number of vertices $|V|$. The second finite set is A, and contains unordered pairs of vertices, called edges. If $\alpha = \{x_1, x_2\}$ is an edge, then α functions as connections of the vertices x_1 and x_2.

The concepts of graph theory can be applied to thermal modeling; in this case, the set V equals the set of individual thermal zones Z. The order of the graph equals the number of thermal zones m. The set A, which provides information about the connections between vertices, can be replaced by the contact matrix u. The Equation (1) shows this representation.

$$G = (V, A) = (Z, u) \tag{1}$$

The set Z includes all arbitrarily enumerated thermal zones, and each element of this set is a list of surfaces defining a thermal zone for this model. Equations (2) and (3) present the structures of the set, using the element Z as the set of surfaces defining a single thermal zone.

$$Z = \{Z_1, Z_2, \ldots, Z_m\} \tag{2}$$

$$Z_i = S_{i,1}, S_{i,2}, \ldots, S_{i,n_i} \quad i = 1, 2, \ldots, m \tag{3}$$

The contact matrix u is a matrix that illustrates the physical organization of thermal zones. This matrix allows one to visually identify which zones share a wall or surface and which do not. Each element of the matrix represents a group of surfaces to allow connection between two zones across multiple surfaces. This situation is particularly common due to contact with the environment. This organization allows the creation of equivalent resistances $Ru_{i,j}$ that contribute to the main coefficients in the mathematical model.

The contact matrix is a matrix with $m \times m$—the Equation (4) shows its structure. Each row corresponds to the relationship between a single zone and all other zones in the system. The subscripts of each element define the surfaces connecting two different zones. For example, the element $u_{2,3}$ is the set of surfaces connecting thermal zones two and three. In the cases of elements with equal subscripts, such as $u_{1,1}$ or $u_{2,2}$, they are the set of surfaces connecting the studied zone with the surroundings [46–48].

$$u = \begin{bmatrix} u_{1,1} & u_{1,2} & \cdots & u_{1,m} \\ u_{2,1} & u_{2,2} & \cdots & u_{2,m} \\ \vdots & \vdots & \ddots & \vdots \\ u_{m,1} & u_{m,2} & \cdots & u_{m,m} \end{bmatrix} \tag{4}$$

For the proposed model, some sets must be defined by the expression $N = m(m+1)$. Each surface of these sets is related to a thermal resistance according to the Equation (5), using L as the wall thickness, kt for the thermal conductivity, and h as the convection

coefficient. The convection coefficient is defined as infinite for the contact surfaces between two zones.

$$R_j = \frac{L_j}{2 \cdot kt_j \cdot S_j} + \frac{1}{h \cdot S_j} \quad j = 1, 2, \ldots, n \tag{5}$$

The Equation (6) shows the relation between the surfaces of each thermal zone and the equivalent resistance defined by the association in the contact matrix, which means that there is a relation between the surface and the thermal resistance $S_{i,j} \mapsto R_{i,n}$. The sets Z_i and u can be understood as sets of resistances.

$$Z_i \Rightarrow \begin{cases} \left.\begin{array}{l} S_{i,1} \rightarrow R_{i,1} \\ S_{i,2} \rightarrow R_{i,2} \\ S_{i,3} \rightarrow R_{i,3} \end{array}\right\} \Rightarrow u_{i,1} \rightarrow Ru_{i,1} \\ \left.\begin{array}{l} S_{i,4} \rightarrow R_{i,4} \\ S_{i,5} \rightarrow R_{i,5} \end{array}\right\} \Rightarrow u_{i,2} \rightarrow Ru_{i,2} \\ \left.\begin{array}{c} \vdots \\ S_{i,n_i} \rightarrow R_{1,n_i} \end{array}\right\} \Rightarrow u_{i,m} \rightarrow Ru_{i,m} \end{cases} \tag{6}$$

Another set of resistances is defined by Rw_i and represents the combination of all internal walls of each thermal zone. This value must be calculated with all elements of the subset Z_i. In this article the notation $|Z_i|$ should be understood as referring to all resistances in the subset Z_i. Equation (7) shows the procedure for calculating Rw_i.

$$Rw_i = \frac{\prod_{k=1}^{|Z_i|} R_k}{\sum_{h=1}^{|Z_i|} \frac{\prod_{k=1}^{|Z_i|} R_k}{R_h}} \quad i = 1, 2, \ldots, m \tag{7}$$

The calculated resistances Rw_i and $Ru_{i,j}$ are used to define the mathematical model. This model corresponds to the 2R2C structure from the lumped parameters technique. The method generates two differential equations for each thermal zone, as presented in Equations (8) and (9).

$$Cw_i \dot{Tw}_i = \frac{T_i}{Rw_i} + \sum_{z=1}^{m} \alpha_{z,i} Tw_z + \beta_i T_{ex} + \phi_i T_{ud} \tag{8}$$

$$Cr_i \dot{T}_i = -\frac{T_i}{Rw_i} + \frac{Tw_i}{Rw_i} \tag{9}$$

The parameters α, β, and ϕ represent the heat transfer coefficients between the different thermal zones and the environment. The α coefficients show the contribution of each thermal zone over a single zone. The β coefficient is the resistance to heat transfer with the surroundings. Finally, the ϕ coefficient is dedicated to regulating the heat transfer through roof and floor. The α and β coefficients must be calculated considering the next two cases:

- Case 1: subscripts $i = j \Rightarrow \alpha_{i,j} = \frac{1}{Rw_i} + \sum_{k=1}^{n} \frac{1}{Ru_{i,k}} \ \wedge \ \beta_i = \frac{1}{Ru_{i,j}} + \frac{1}{Rg}$
- Case 2: subscripts $i \neq j \Rightarrow \alpha_{i,j} = \frac{1}{Ru_{i,j}}$

The state variables of the model are the internal temperature (T) and the wall temperature (T_w). The constants Cw_i and Cr_i represent the thermal capacity to store energy. The variable T_{ex} is dependent on the ambient temperature [49]. The ceiling and floor temperature is summarized as $T_{ud} = T_{floor} = T_{ceiling}$; these temperatures are controlled by the coefficient ϕ. In cases where the thermal zones are surrounded by air, T_{ud} and T_{ex} are equal and the coefficient β can be used exclusively to include the environmental temperature.

Finally, the constants Cw and Cr are the heat capacity of the interior air and walls. They can be calculated with the Equation (10), taking ρ as the density, Ce as the specific heat, and V as the volume of the material, using the properties of the indoor air or walls as appropriate.

$$C = \rho \cdot Ce \cdot V \tag{10}$$

The alpha coefficient can be organized as a vector, in which the individual contributions of the other zones on a single zone are included. The coefficient is a vector $\alpha_i = \begin{bmatrix} \alpha_{i,1} & \alpha_{i,2} & \cdots & \alpha_{i,m} \end{bmatrix}$. For example, to represent the first thermal zone α_1, the element $\alpha_{1,2}$ shows the heat transferred from the second thermal zone to the first. $\alpha_{i,j} = 0$ indicates that the two zones are not physically connected.

The coefficients α can be arrays between the resistances Rw_i and $R_{i,j}$. $R_{i,j}$ is the equivalent resistance resulting from simplifying all the resistances associated with each element of the contact matrix. Equation (11) allows to calculate the equivalent resistance using i and j as values between 1 and m.

$$Ru_{i,j} = \frac{\prod_{k=1}^{|u_{i,j}|} R_k}{\sum_{h=1}^{|u_{i,j}|} \frac{\prod_{k=1}^{|u_{i,j}|} R_k}{R_h}} \quad \forall \{i = 1, 2, \ldots, m \wedge j = 1, 2, \ldots, m\} \tag{11}$$

Finally, for each thermal zone it is necessary to calculate the roof and floor resistances (R_{floor} and $R_{ceiling}$). In cases with equal materials, the resistance values are equal and must be calculated using surface arrangements in the studied zone as shown in the following example expression:

$$R_{floor} = R_{roof} = Rg_i(S) = \sum S_x \times S_y - \sum S_z \times S_w \quad \forall \{x, y, z, w\} \exists Z_i \tag{12}$$

2.2. Experimental Case Setup

To demonstrate the mathematical models generated with the methodology of this article, an experiment with a reduced scale model was developed. The experiment measured the temperature of a miniature model of a residential apartment. The building under study consists of three bedrooms, two bathrooms, a living room, and a kitchen, as shown in Figure 3. The overall dimensions of the building are nine meters long, six meters wide, and three meters high.

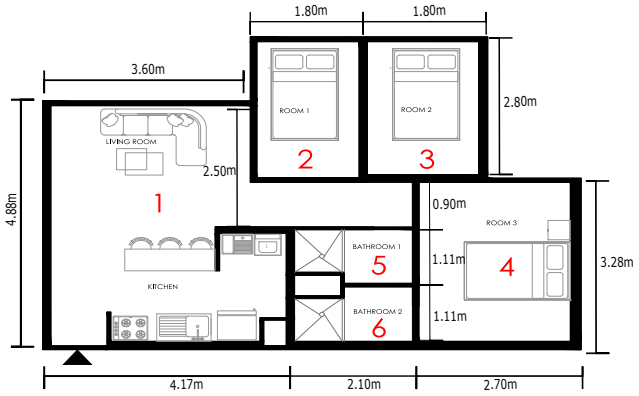


Figure 3. Structure of the studied building.

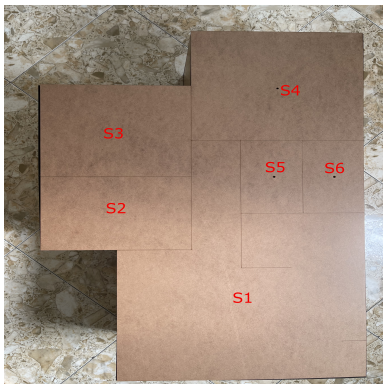
The construction contains six zones of interest or thermal zones, since the living room and the kitchen can be considered a single zone, as there are no relevant separations between them. In the same way, to adjust the developed models, a 1:10 scale model is built. The design is carried out in AutoCAD [50], where small irregular structures, such as the separation wall of the bathrooms, are eliminated in order to keep the structure as uniform as possible.

Figure 4 shows the model constructed for this experiment. Each wall is a 3 mm thick medium density fiberboard (MDF); the choice of this material is due to its favorable physical and mechanical properties, availability, and low commercial cost. In addition, this material is laser cut to obtain a stable, resistant, and accurate structure for greater precision and reliability in the measurements taken. It is necessary to state that this experimental test is only a tool to demonstrate that the mathematical models produced with the proposed

methodology are physically feasible. In future cases where it is applied to real buildings, the model coefficients will change, but the structure of the mathematical model will be very similar.



(a) Model from a close-up view (b) Model from a zenithal view



(c) Sensors ubication

Figure 4. Reduced-scale model.

The physical characteristics that define the thermal capacity and thermal conduction for the medium-density fiberboard are specific heat (Ce = 1700 $\frac{\mathrm{J}}{\mathrm{kgK}}$), thermal conductivity ($kt = 0.3\ \frac{\mathrm{w}}{\mathrm{m}}$), and density ($\rho = 0.75\ \frac{\mathrm{g}}{\mathrm{cm}^3}$). Similarly, the thermal characteristics for the contained air used are $C_e = 1000\ \frac{\mathrm{J}}{\mathrm{kg}}\mathrm{m}^3$, $kt = 1.4\ \frac{\mathrm{w}}{\mathrm{m}^3}$, and $\rho = 1.2\ \frac{\mathrm{kg}}{\mathrm{m}^3}$.

To evaluate the thermal behavior of each zone and of the entire reduced scale model, an internal heat source, namely a 100 w incandescent lamp, is introduced in zone 1. The lamp is active for 120 min and inactive for the next 180 min. The heat source is controlled by a relay device, which is activated or deactivated by an Arduino board according to the predefined charge and discharge cycles. This Arduino board functions as a central control unit, regulating the operation of the load, receiving the information from the sensors, and storing it on an SD card. To measure the temperature, seven ds18B20 sensors are connected, one for each thermal zone and one for the ambient temperature. The sensors can provide measurements over a range of −55 °C to +125 °C, maintaining an accuracy of 0.5 °C from −10 °C to +85 °C. In the range from −30 °C to 100 °C the accuracy is 1 °C. The maximum accuracy is 2 °C in the maximum measurement range. The sensor is sealed in a metal cap that allows it to be immersed in liquid or protected from the weather. Table 1 contains the electronic elements used during the experiment.

Table 1. Electronic components.

Quantity	Element	Reference
1	Control card	Arduino Uno
7	Temperature sensor	Ds18b20
1	Relay	JQC-3FF-S-Z
1	Heat source	100 w incandescent bulb
1	Memory device	MicroSD card adapter and 256 Mb MicroSD

2.3. Methodology Implementation on Case

The selected case study has six thermal zones. This system was analyzed using the methodology derived from the graph theory and the clustered parameters previously described. The first step in this methodology is to define the two elements of the graph $G = (Z, u)$, taking Z as the set of thermal zones and u as the u contact information. For this specific case the set Z can be defined as follows:

$$Z = \{Z_1, Z_2, Z_3, Z_4, Z_5, Z_6\} \tag{13}$$

Figure 5 shows the numbering of the surfaces in each zone. The numbering presented in Figure 3 is retained to assign the name of each thermal zone. That is, room n is equivalent to Z_n.

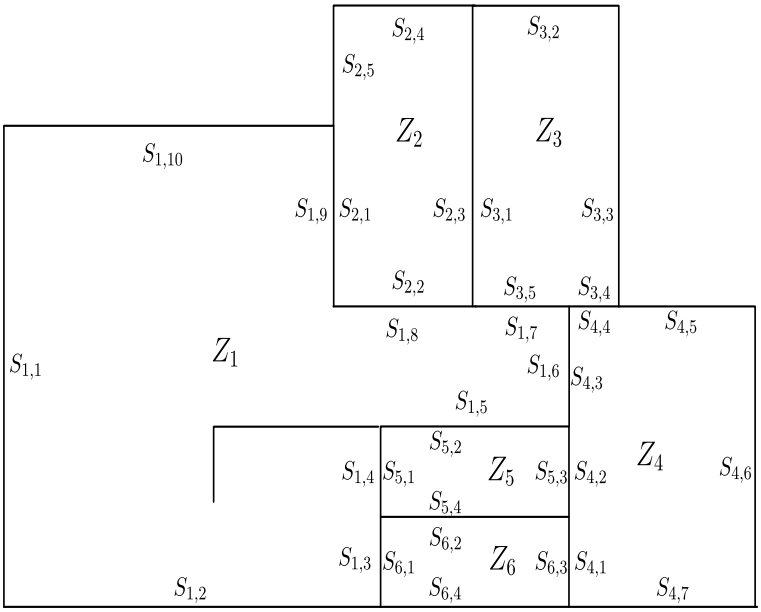


Figure 5. Thermal zones with surfaces numbering.

Equations (14)–(19) show the sets of surfaces for each individual thermal zone. Using Equation (7) the R_w term can be calculated for all sets.

$$Z_1 = \{S_{1,1}, S_{1,2}, S_{1,3}, S_{1,4}, S_{1,5}, S_{1,6}, S_{1,7}, S_{1,8}, S_{1,9}, S_{1,10}\} \tag{14}$$

$$Z_2 = \{S_{2,1}, S_{2,2}, S_{2,3}, S_{2,4}, S_{2,5}\} \tag{15}$$

$$Z_3 = \{S_{3,1}, S_{3,2}, S_{3,3}, S_{3,4}, S_{3,5}\} \tag{16}$$

$$Z_4 = \{S_{4,1}, S_{4,2}, S_{4,3}, S_{4,4}, S_{4,5}, S_{4,6}, S_{4,7}\} \tag{17}$$

$$Z_5 = \{S_{5,1}, S_{5,2}, S_{5,3}, S_{5,4}\} \tag{18}$$

$$Z_6 = \{S_{6,1}, S_{6,2}, S_{6,3}, S_{6,4}\} \tag{19}$$

The second element of the graphical modeling is the contact matrix presented in Equation (20). This matrix shows the physical disconnection between some thermal zones. For example, the terms in the second, third, fourth, and fifth rows are equal to zero because Zone 2 does not share a surface area with Zones 4, 5, and 6.

$$u = \begin{bmatrix} u_{1,1} & u_{1,2} & u_{1,3} & u_{1,4} & u_{1,5} & u_{1,6} \\ u_{2,1} & u_{2,2} & u_{2,3} & 0 & 0 & 0 \\ u_{3,1} & u_{3,2} & u_{3,3} & u_{3,4} & 0 & 0 \\ u_{4,1} & 0 & u_{4,3} & u_{4,4} & u_{4,5} & u_{4,6} \\ u_{5,1} & 0 & 0 & u_{5,4} & 0 & u_{5,6} \\ u_{6,1} & 0 & 0 & u_{6,4} & u_{6,5} & u_{6,6} \end{bmatrix} \tag{20}$$

Each element of the contact matrix corresponds to a thermal resistance according to Equation (7). The surface subsets for each element of the matrix are presented in (21). Maintaining the rule that the impact of one thermal zone on another is bidirectional, therefore, $u_{i,j} = u_{j,i}$.

$$\begin{array}{cc} u_{1,1} = \{S_{1,1}, S_{1,2}, S_{1,10}\} & u_{1,2} = u_{2,1} = \{S_{1,8}, S_{1,9}\} = \{S_{2,1}, S_{2,2}\} \\ u_{1,3} = u_{3,1} = \{S_{1,7}\} = \{S_{3,5}\} & u_{1,4} = u_{4,1} = \{S_{1,6}\} = \{S_{4,3}\} \\ u_{1,5} = u_{5,1} = \{S_{1,5}\} = \{S_{5,2}\} & u_{1,6} = u_{6,1} = \{S_{1,3}\} = \{S_{6,1}\} \\ u_{2,2} = \{S_{2,4}, S_{2,5}\} & u_{2,3} = u_{3,2} = \{S_{2,3}\} = \{S_{3,1}\} \\ u_{3,3} = \{S_{3,2}, S_{3,3}\} & u_{3,4} = u_{4,3} = \{S_{3,4}\} = \{S_{4,4}\} \\ u_{4,4} = \{S_{4,5}, S_{4,6}, S_{4,7}\} & u_{4,5} = u_{5,4} = \{S_{4,2}\} = \{S_{5,3}\} \\ u_{5,5} = \{0\} & u_{5,6} = u_{6,5} = \{S_{5,4}\} = \{S_{6,2}\} \\ u_{6,6} = \{S_{6,4}\} & \end{array} \tag{21}$$

Following the methodology shown in section two, Equations (7) and (11) allow to calculate the resistances Rw_i and $Ru_{i,j}$. For example, the first element of the groups Z and u are calculated in Equations (22) and (23). Earlier, it was mentioned that the notations $|Z_1|$ and $|u_{1,1}|$ are used to call all resistances calculated with the surfaces of that subset.

$$Z_1 \Rightarrow Rw_1 = \frac{\prod_{k=1}^{|Z_1|} R_{1,k}}{\sum_{h=1}^{|Z_1|} \frac{\prod_{k=1}^{|Z_1|} R_{1,k}}{R_{1,h}}} \tag{22}$$

$$u_{1,1} \Rightarrow Ru_{1,1} = \frac{\prod_{k=1}^{|u_{1,1}|} R_{1,k}}{\sum_{h=1}^{|u_{1,1}|} \frac{\prod_{k=1}^{|u_{1,1}|} R_{1,k}}{R_{1,h}}} \tag{23}$$

To calculate all the mathematical model coefficients the process must be repeated with all the subsets in u and Z. For example, in this specific case the coefficients $\alpha_{1,1}$, $\alpha_{1,2}$, and β_1 are calculated as $\alpha_{1,1} = \frac{1}{Rw_1} + \frac{1}{R_{1,1}} + \frac{1}{R_{1,2}} + \frac{1}{R_{1,3}} + \frac{1}{R_{1,4}} + \frac{1}{R_{1,5}} + \frac{1}{R_{1,6}}$, $\alpha_{1,2} = \frac{1}{R_{1,2}}$ and $\beta_1 = \frac{1}{R_{1,1}} + \frac{1}{Rg_1}$.

The visual representation for this study case is presented in Figure 6. In this case, it can be classified as an extraverted edge.

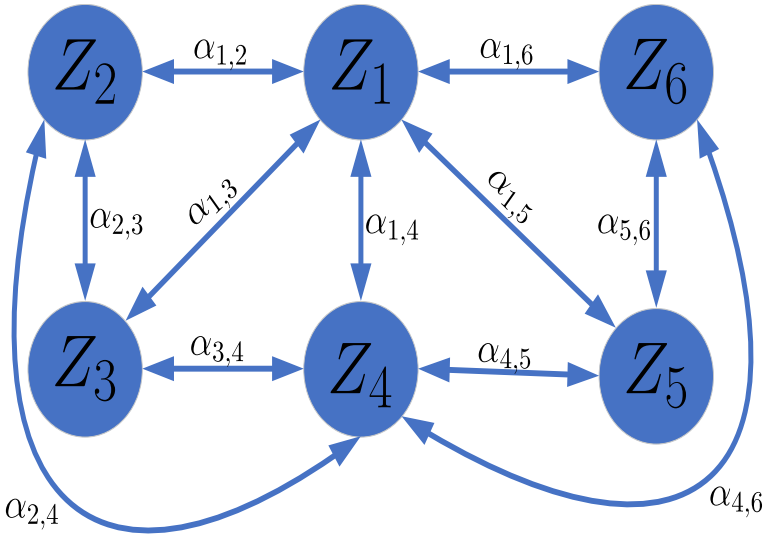


Figure 6. Graph for the study case.

The mathematical model is presented in Equations (24)–(35). In this case, the model is surrounded by air, including the roof and floor surfaces, which increases the impact of environmental temperature and simplifies the model by eliminating the ϕ terms. When there are different temperatures or other thermal zones in contact with the roof or floor surfaces, this simplification is not possible.

In Equation (25), Q term is included to add the internal heat source.

$$Cw_1\dot{Tw}_1 = \frac{T_1}{Rw_1} - \alpha_{1,1}Tw_1 + \alpha_{1,2}Tw_2 + \alpha_{1,3}Tw_3 + \alpha_{1,4}Tw_4 + \alpha_{1,5}Tw_5 + \alpha_{1,6}Tw_6 + \beta_1 T_{ex} \tag{24}$$

$$Cr_1\dot{T}_1 = -\frac{T_1}{Rw_1} + \frac{Tw_1}{Rw_1} + Q \tag{25}$$

$$Cw_2\dot{Tw}_2 = \frac{T_2}{Rw_2} + \alpha_{2,1}Tw_1 - \alpha_{2,2}Tw_2 + \alpha_{2,3}Tw_3 + \beta_2 T_{ex} \tag{26}$$

$$Cr_2\dot{T}_2 = -\frac{T_2}{Rw_2} + \frac{Tw_2}{Rw_2} \tag{27}$$

$$Cw_3\dot{Tw}_3 = \frac{T_3}{Rw_3} + \alpha_{3,1}Tw_1 + \alpha_{3,2}Tw_2 - \alpha_{3,3}Tw_3 + \alpha_{3,4}Tw_4 + \beta_3 T_{ex} \tag{28}$$

$$Cr_3\dot{T}_3 = -\frac{T_3}{Rw_3} + \frac{Tw_3}{Rw_3} \tag{29}$$

$$Cw_4\dot{Tw}_4 = \frac{T_4}{Rw_4} + \alpha_{4,1}Tw_1 + \alpha_{4,3}Tw_3 - \alpha_{4,4}Tw_4 + \alpha_{4,5}Tw_5 + \alpha_{4,6}Tw_6 + \beta_4 T_{ex} \tag{30}$$

$$Cr_4\dot{T}_4 = -\frac{T_4}{Rw_4} + \frac{Tw_4}{Rw_4} \tag{31}$$

$$Cw_5\dot{Tw}_5 = \frac{T_5}{Rw_5} + \alpha_{5,1}Tw_1 + \alpha_{5,4}Tw_4 - \alpha_{5,5}Tw_5 + \alpha_{5,6}Tw_6 + \beta_5 T_{ex} \tag{32}$$

$$Cr_5\dot{T}_5 = -\frac{T_5}{Rw_5} + \frac{Tw_5}{Rw_5} \tag{33}$$

$$Cw_6\dot{Tw}_6 = \frac{T_6}{Rw_6} + \alpha_{6,1}Tw_1 + \alpha_{6,4}Tw_4 + \alpha_{6,5}Tw_5 - \alpha_{6,6}Tw_6 + \beta_6 T_{ex} \tag{34}$$

$$Cr_6\dot{T_6} = -\frac{T_6}{Rw_6} + \frac{Tw_6}{Rw_6} \tag{35}$$

The coefficients α, β, and Rw can be estimated from their physical properties, but the convection coefficients at each wall must be precisely matched to the conditions of this experiment. In addition, considering the methodology employed in this experiment, the loading and unloading phases produced different sets of coefficients.

3. Results

Algorithm 1 is presented to illustrate the mathematical model tuning process. This algorithm was implemented in Matlab software and was based on the predefined Pattern Search function. To use this algorithm it is necessary to provide initial values for the coefficients and a search range. Additionally the program must have experimental measurements to adjust the coefficients in the defined range. Specifically, the function has 28 parameters to tune, distributed in 22 alpha coefficients and 6 beta coefficients.The adjustment algorithm starts from the initial values and executes the mathematical model provided, once it calculates the values in simulation it compares them with the experimental results to determine the error of each thermal zone. Finally, the objective function is the sum of the errors between simulation and experimental of each thermal zone, i.e., $F_{obj} = \sum_{i=1}^{6} e_i$.

Algorithm 1 Tuning algorithm

Inputs: Initial parameters, search range, environment temperature, measured temperatures

$[\alpha_1, \alpha_2, \ldots, \alpha_m, \beta_1, \beta_2 \ldots \beta_m, \phi_1, \phi_2, \ldots, \phi_m]$ = PatternSearch

$$[e_1, e_2, e_3, e_4, e_5, e_6] = \text{MathModel}(\alpha_1, \alpha_2, \ldots, \alpha_m, \beta_1, \beta_2 \ldots \beta_m, \phi_1, \phi_2, \ldots, \phi_m)$$

$$\begin{aligned}
\dot{Tw_1} &= \alpha_{1,1}Tw_1 + \alpha_{1,2}Tw_2 + \cdots + \alpha_{1,m}Tw_m + \beta_1 T_{ex} + \phi_1 T_{ud} \\
\dot{Tw_2} &= \alpha_{2,1}Tw_1 + \alpha_{2,2}Tw_2 + \cdots + \alpha_{2,m}Tw_m + \beta_2 T_{ex} + \phi_2 T_{ud} \\
&\vdots \\
\dot{Tw_m} &= \alpha_{m,1}Tw_1 + \alpha_{m,2}Tw_2 + \cdots + \alpha_{m,m}Tw_m + \beta_m T_{ex} + \phi_m T_{ud} \\
e_1 &= T_{1_{measured}} - T_{1_{simulation}} \\
e_2 &= T_{2_{measured}} - T_{2_{simulation}} \\
&\vdots \\
e_6 &= T_{6_{measured}} - T_{6_{simulation}} \\
F_{objetive} &= min\left\{\sum_{i_1}^{6} e_i\right\}
\end{aligned}$$

The process of adjusting the system to the loading and unloading phase must be done individually. Only one phase is considered to calculate the coefficients and they are reused to compare with the following cycles. The results of the adjustment process are presented in Tables 2 and 3.

Table 2. α coefficients in charge phase.

i\j	1	2	3	4	5	6
1	0.5	0.12	0.012	0.01	0.01	0.135
2	0.12	0.6	0.51	0	0	0
3	0.012	0.51	2.5742	0.51	0	0
4	0.01	0	0.51	2.1406	0.01	0.012
5	0.01	0	0	0.01	1	0
6	0.135	0	0	0.012	0	2.666

Table 3. α coefficients in discharge phase.

i\j	1	2	3	4	5	6
1	0.8	0.0001	0.0002	0.0002	0.0001	0.00013
2	0.0001	0.85	0.0003	0	0	0
3	0.0002	0.0003	0.3005	0.0005	0	0
4	0.0002	0	0.0005	0.7625	0.0001	0.00012
5	0.0001	0	0	0.0001	0.8217	0.0001
6	0.00013	0	0	0.00012	0.0001	1.35

Table 4 show the β and Rw coefficients for the charge and discharge phases. Tables 1–3 contain all the necessary elements to simulate the mathematical model.

Table 4. Coefficients in charge and discharge phase.

		i					
		1	**2**	**3**	**4**	**5**	6
Charge phase	$\frac{1}{Rw_i}$	0.0074	0.0226	0.9073	0.9790	0.9064	0.9983
	β_i	0.5544	0.1312	0.5997	0.6267	0.0922	0.4594
Discharge phase	$\frac{1}{Rw_i}$	0.634	0.8024	0.231	0.71	0.8	0.03022
	β_i	0.1743	0.0475	0.0675	0.0515	0.0222	0.5105

The simulation time was more than 1500 min for this mathematical model, exactly 25 h. The system can be classified as MIMO (multiple inputs and multiple outputs), according to the control theory [51]. We are using the ambient temperature and internal heat source as input. The outputs are six internal temperatures, one for each zone. Figures 7–12 show the simulated internal temperature for the thermal zones with the blue line. The red and green lines represent the experimentally recorded internal and ambient temperature.

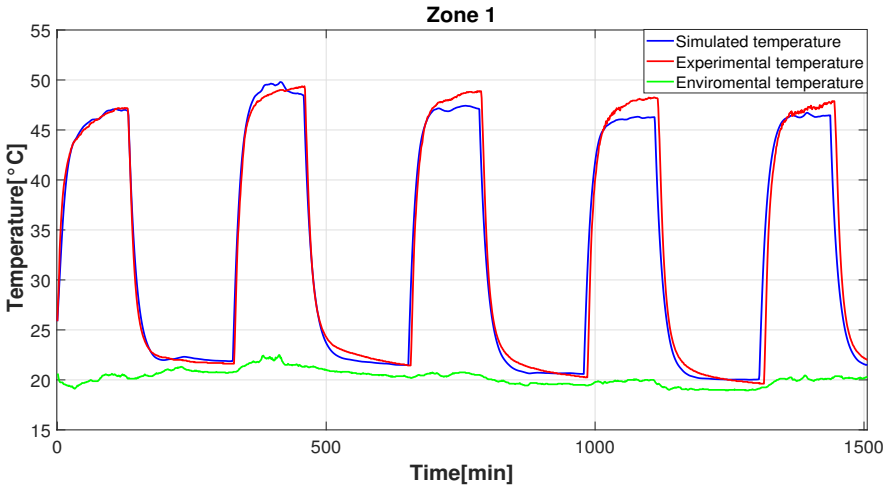


Figure 7. Experimental and simulated temperature for Zone 1.

Figure 7 shows the internal temperature of Zone 1 in simulation and experimentally recorded. The experimental temperature varies in the range of 47.2 to 49.4 °C, the simulation between 46.2 to 49.8 °C, and the ambient temperature varies in the range of 19 to 22.5 °C. The highest temperature levels recorded in the internal temperature coincide with

the peaks of the environmental temperature. During these moments of high environmental temperature, heat transfer to the environment is reduced, which allows the system to accumulate additional thermal energy and reach higher internal temperature peaks. The point of maximum internal temperature is reached around the 400th minute, the second point of maximum internal temperature is around the 700th minute, directly coinciding with the points of maximum ambient temperature.

During the process of adjusting the mathematical model, the high impact of environmental conditions was evident. Due to the fact that the walls in all cases were of the same thickness and material, it can be seen that the weight of the beta coefficient is much higher in the zones with greater surface area exposed to the environment. For example, in the loading phase, the beta coefficient of Zone 1 is the highest, because it is the thermal zone with the largest surface area in contact with the environment, while Zone 5 has the smallest exposed surface area and consequently has the lowest beta coefficient.

Figures 8–12 show the internal and experimental temperatures for Zones 2, 3, 4, 5, and 6, respectively. In all these cases, the temperature levels are lower because they do not have an internal heat source, but they are influenced by the charging and discharging cycle of the heat source in Zone 1. Additionally, they present variations in their maximum values during the charging phase according to the variation of the environmental conditions previously described.

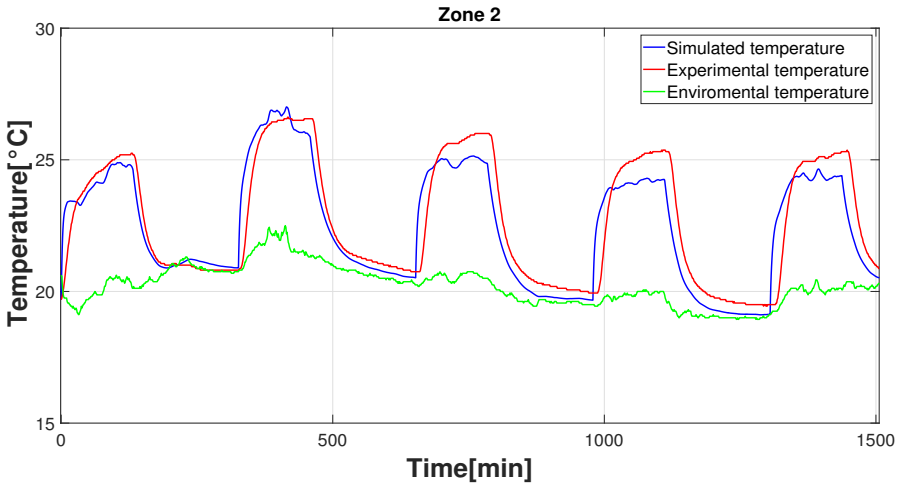


Figure 8. Experimental and simulated temperature for Zone 2.

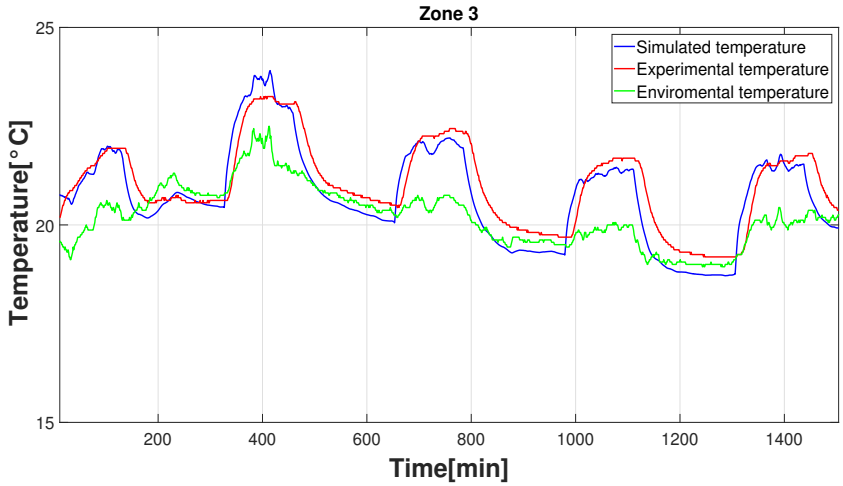


Figure 9. Experimental and simulated temperature for Zone 3.

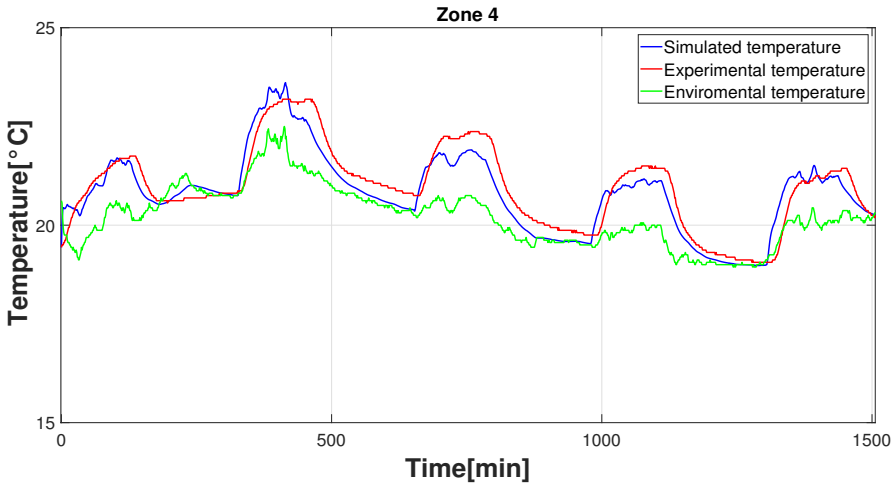


Figure 10. Experimental and simulated temperature for Zone 4.

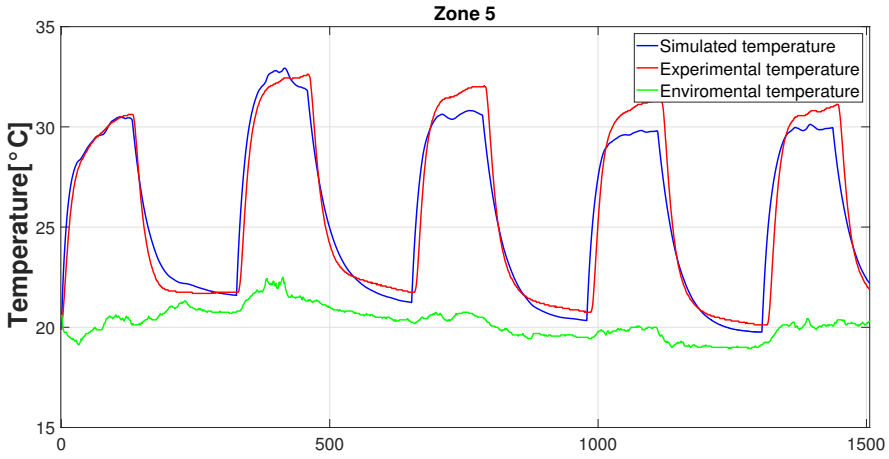


Figure 11. Experimental and simulated temperature for Zone 5.

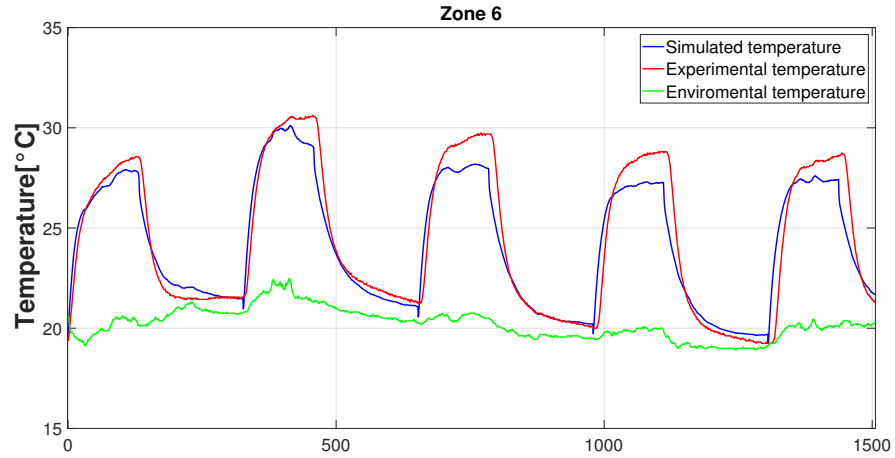


Figure 12. Experimental and simulated temperature for Zone 6.

Pattern search is the optimization algorithm used to adjust the parameters of the mathematical model. The objective function is the sum of the individual errors between the simulated temperature and its corresponding experimental temperature, so that $F_{obj} = sum_{i=1}^{6} e_i$. The simulation and recorded data allow the accuracy of the mathematical model to be evaluated.

However, the tuning process starts initially by considering only one thermal zone, in order to obtain the best parameters for Zone 1. The second step consists of adding the experimental data from the second zone and uses the first results as initial conditions. The third step uses the initial conditions of Zones 1 and 2 to adjust the results. This process was continued until all six outputs were reached, looking for the best simulation result in relation to the experimental data. Figure 13 shows the percentage errors between the simulation and experimental results. The errors vary from 1.88% to 6.63% and maintain an average of 4.0%, which allows us to conclude that the mathematical modeling strategy can represent the case study with an acceptable level of error.

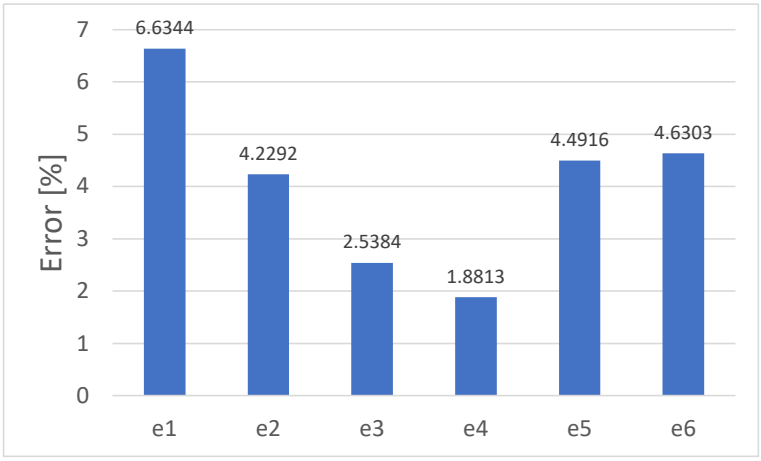


Figure 13. Errors between simulation and experimental results.

Finally, a sensitivity analysis was applied to the mathematical model. The analysis is based on determining the impact of each α coefficient on temperature at a single temperature. We selected Zone 1 because it is the only zone that is in contact with the other five zones and contains the heat source. The α coefficients were changed from their values in Table 1. The new value took the original value and modified it with a range of variations of $\pm$5%, $\pm$10%, and $\pm$15%.

Figure 14 shows the results of the analysis, using the x as the input perturbations and the y-axis for the percent temperature variation. Based on the results of the sensitivity analysis, it is possible to state that all the coefficients α have a similar impact on the internal temperature in Zone 1. The slight variation of $\alpha_{1,6}$ can be explained by the proximity to the internal heat source and does not significantly change the conclusions.

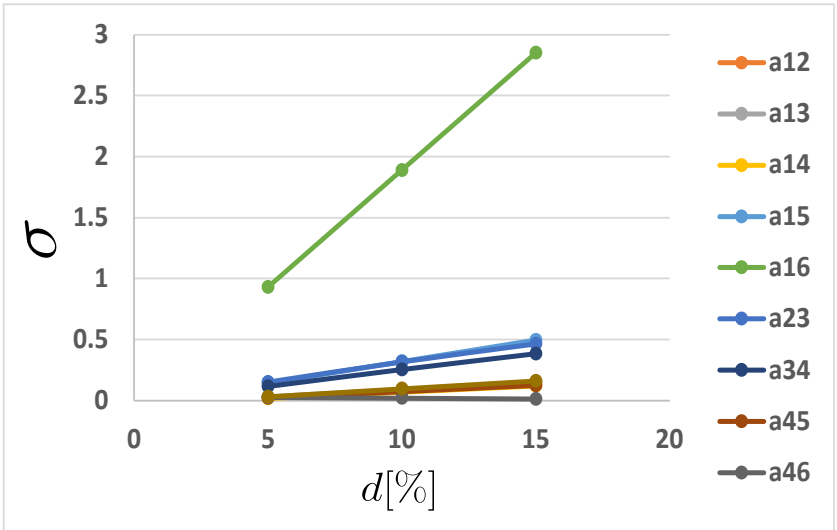
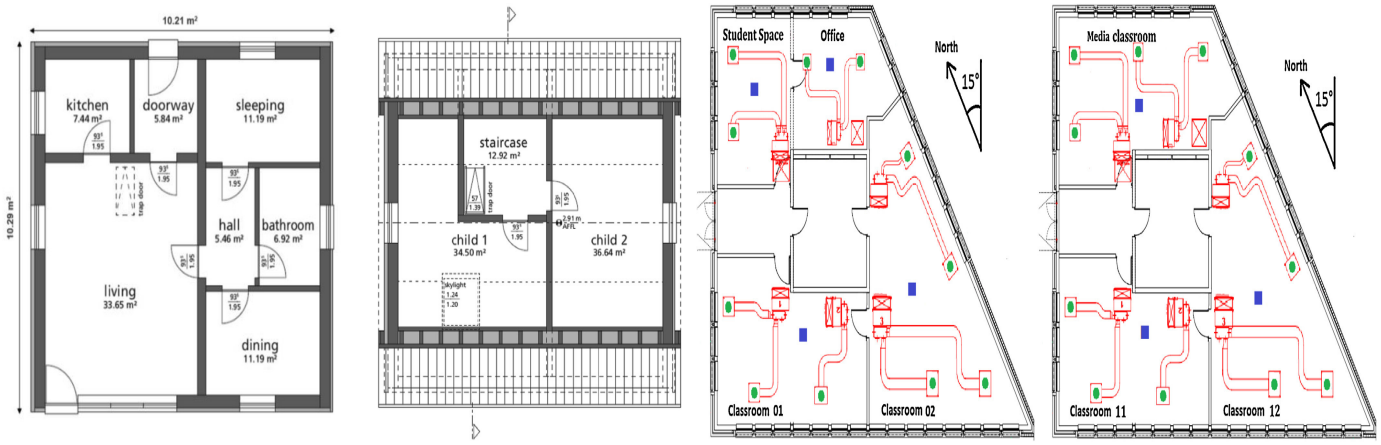


Figure 14. Sensibility analysis for α coefficients.

4. Discussion

Many investigations of single and square thermal zones can be found in the literature [40,52–54]. However, most offices and residential buildings are composed of multiple thermal zones connected by walls, windows or doors. This situation makes it necessary to formulate and use multiple thermal zone models, which represent a better approximation to real buildings. The methodology presented in this paper can be classified as gray box models. This type of model provides insight into the impact of wall materials and structures on specific variables. These relationships are difficult to understand in investigations using black box models and specialized software. For example, Figure 15a shows the floor plan of a house located at the Fraunhofer Institute for Building Physics in Holzkirchen, Germany. This building is used as a case study in [48] and is analyzed with the commercial program TRNSYS. However, Figure 15b shows the floor plan of the Renewable Energies department of the engineering school Polytech Montpellier, located in the city of Perpignan (South of France). In this case, the geometry of the thermal zones is not square and requires the use of black box models implemented in specialized programs such as EnergyPlus [55].



(a) Fraunhofer Institute for Building Physics in Holzkirchen (b) Engineering school Polytech Montpellier

Figure 15. Residential and offices planes.

Using the methodology presented in this article, the case studies presented in Figure 15 can be analyzed without the need for specialized programs. With this methodology, any type of structure can be studied, regardless of whether they are square, circular, or other geometries. In addition, individual wall reinforcements can be considered as cladding solutions and their impact on the overall thermodynamics.

The proposed methodology is a first version and can still be improved. Evaluating the resulting mathematical model on a real structure can be costly, time consuming, and difficult to control. For this reason, we decided to use similarity theory, building a reduced scale model with similarity conditions in geometry and scaling for structural behavior [56]. This strategy is widely used in prototyping and initial testing of scientific theories [57–60]. The model used in this work has characteristics provided by the material and dimensions of the walls. The low wall thickness, interior air volume, and thermal properties limit the thermal capacity and allow high temperatures to be reached in a short time. These temperatures may exceed comfort levels, but as a test scenario, the reduced scale model provides sufficient information to refine the mathematical model. In a real scenario with a full-scale model, the recorded information allows the model coefficients to be refined. The real model can maintain the same structure as the reduced scale mathematical model, changing only the values and heat sources. In this case, the developed methodology can be classified as a viable tool for structural modeling.

5. Conclusions

The paper presents a methodology for modeling multiple thermal zones, based on graph theory and the lumped parameter technique. The methodology works with different resistance subgroups defined by each thermal zone and the walls between contiguous zones. A residential apartment is used as a case study. The methodology is applied in this case study and generates a MIMO model with 28 parameters, 2 inputs, and 6 outputs. The parameters are coefficients generated from the resistance and thermal capacity of the walls in each zone. The inputs are the environmental temperature and the internal heat source. Finally, the outputs are the six internal temperatures, one for each zone. An experiment is proposed and executed to verify the accuracy of the mathematical model. The research is based on reduced scale models. A model of the apartment chosen as a study was built. The reduced model has a 10 to 1 ratio with the original model, and an internal heat source was considered to create heat flows between the different zones. The internal load is turned on and off generating load and unload phases for the internal temperatures. The internal temperatures reach levels above the comfort range, but facilitate the construction of the mathematical model and reduce the data collection period. In a full-scale experiment, the heat source must be extremely large and excessive energy consumption would result. In addition, environmental conditions may introduce additional problems in the initial testing of the methodology. The experimental data allowed to fit all 28 parameters and achieve an error of less than 6.6% for all thermal zones. The performance of the mathematical model is acceptable by comparison with the experimental data, maintaining an average difference of 4.0% between the experimental and simulated data. The experimental data allowed to fit the 28 parameters and to achieve an error of less than 6.6% for all thermal zones. Finally, the modeling technique allows the construction of a graphical matrix with six nodes and the identification of the different ratio coefficients. The parameters of the mathematical model are calculated during the loading and unloading phases. In addition, the impact of each coefficient on the overall performance is evaluated.

In the future, the modeling technique will have to overcome some limitations, such as solar radiation gains. This type of source is analyzed as a variable heat source and may affect each zone differently, increasing the complexity of the adjustment process. Another possible improvement is the application of the methodology in several apartments at the same time or in buildings with several levels. On the other hand, experiments can be performed to improve the adjustment process by including more elements such as windows and multiple internal heat sources.

Author Contributions: Conceptualization and methodology: P.F.d.C., J.A.T.-G. and F.F.; experiment development and data collection: J.A.A.-G.; data analysis and simulations: F.F.; writing—original draft preparation: J.A.A.-G. and F.F.; funding acquisition: P.F.d.C. and J.A.T.-G. The authors consider that all of them contributed equally to this work. All authors have read and agreed to the published version of the manuscript.

Funding: The APC was financed through a call to support the publication of articles in international journals approved in the national bibliographic index PUBLINDEX, of the Universidad del Magdalena in accordance with its government plan 2020-2024.

Data Availability Statement: Not applicable.

Acknowledgments: Pedro Fernández de Córdoba acknowledges the grant PID2021-128676OB-I00 funded by FEDER/MCIN.

Conflicts of Interest: The authors declare no conflict of interest.

Sample Availability: Samples of the compounds are available from the authors.

Nomenclature

The following abbreviations are used in this manuscript:

Ce	Specific heat	$\frac{kJ}{kh \cdot K}$
Cr	Air thermal capacity	$\frac{kJ}{K}$
Cw	Walls thermal capacity	$\frac{kJ}{K}$
G	Graph arrangement	
h	Convection coefficient	$\frac{kJ}{h \cdot m \cdot K}$
kt	Thermal conductivity	$\frac{kJ}{h \cdot m^2 \cdot K}$
L	Wall thickness	m
m	Number of thermal zones	
n	Number of surfaces per zone	
$S_{i,j}$	Superficial area	m^2
u	Contact matrix	
R_j	Thermal resistance	$\frac{h \cdot K}{kJ}$
R_g	Thermal resistance for floor and ceiling	$\frac{h \cdot K}{kJ}$
Ru	Resistance equivalent	$\frac{h \cdot K}{kJ}$
Rw	Inner envelope wall	$\frac{h \cdot K}{kJ}$
T	Internal temperature	°C
T_{ext}	Environmental temperature	°C
T_{ud}	Floor and ceiling temperature	°C
Tw	Walls temperature	°C
V	Volume	m^3
Z	Thermal zone	
α	Heat transfer coefficient between zones	$\frac{kJ}{h \cdot K}$
β	Heat transfer coefficient with environmental conditions	$\frac{kJ}{h \cdot K}$
ϕ	Heat transfer coefficient with ground and floor	$\frac{kJ}{h \cdot K}$
ρ	Density	$\frac{kg}{m^3}$

References

1. ONU. Agenda 2030 y los Objetivos de Desarrollo Sostenible. *Patrim. Econ. Cult. Educ. Para Paz Mec-Edupaz* **2017**, *1*, 48.
2. Harputlugil, T.; de Wilde, P. The interaction between humans and buildings for energy efficiency: A critical review. *Energy Res. Soc. Sci.* **2021**, *71*, 101828. [CrossRef]
3. Asere, L.; Blumberga, A. *Energy Efficiency-Indoor Air Quality Dilemma in Public Buildings*; Elsevier Ltd.: Amsterdam, The Netherlands, 2018; Volume 147, pp. 445–451. [CrossRef]
4. Lu, Y.; Dong, J.; Liu, J. Zonal modelling for thermal and energy performance of large space buildings: A review. *Renew. Sustain. Energy Rev.* **2020**, *133*, 110241. [CrossRef]
5. Czerniawski, T.; Leite, F. Automated digital modeling of existing buildings: A review of visual object recognition methods. *Autom. Constr.* **2020**, *113*, 103131. [CrossRef]
6. Li, Y.; O'Neill, Z.; Zhang, L.; Chen, J.; Im, P.; DeGraw, J. Grey-box modeling and application for building energy simulations—A critical review. *Renew. Sustain. Energy Rev.* **2021**, *146*, 111174. [CrossRef]
7. Fanger, P.O. *Thermal Comfort. Analysis and Applications in Environmental Engineering*; Danish Technical Press: Copenhagen, Denmark, 1970; p. 244.
8. Epstein, Y.; Moran, D.S. Thermal Comfort and the Heat Stress Indices. *Ind. Health* **2006**, *44*, 388–398. [CrossRef]
9. Kaushik, A.; Arif, M.; Tumula, P.; Ebohon, O.J. Effect of thermal comfort on occupant productivity in office buildings: Response surface analysis. *Build. Environ.* **2020**, *180*, 107021. . [CrossRef]
10. Maintaining Thermal Comfort in Indoor Work Environments | SafeWork NSW. Available online: https://www.safework.nsw.gov.au/resource-library/heat-and-environment/maintaining-thermal-comfort-in-indoor-work-environments (accessed on 27 January 2023).
11. Ganesh, G.A.; Sinha, S.L.; Verma, T.N.; Dewangan, S.K. Investigation of indoor environment quality and factors affecting human comfort: A critical review. *Build. Environ.* **2021**, *204*, 108146. [CrossRef]
12. Geng, Y.; Ji, W.; Lin, B.; Zhu, Y. The impact of thermal environment on occupant IEQ perception and productivity. *Build. Environ.* **2017**, *121*, 158–167. [CrossRef]
13. Mitchell, D.; Heaviside, C.; Vardoulakis, S.; Huntingford, C.; Masato, G.; Guillod, B.P.; Frumhoff, P.; Bowery, A.; Wallom, D.; Allen, M. Attributing human mortality during extreme heat waves to anthropogenic climate change. *Environ. Res. Lett.* **2016**, *11*, 074006. [CrossRef]

14. Alshamaila, Y.; Papagiannidis, S.; Alsawalqah, H.; Aljarah, I. Effective use of smart cities in crisis cases: A systematic review of the literature. *Int. J. Disaster Risk Reduct.* **2023**, *85*, 103521. [CrossRef]
15. van Twist, A.; Ruijer, E.; Meijer, A. Smart cities & citizen discontent: A systematic review of the literature. *Gov. Inf. Q.* **2023**. [CrossRef]
16. Mora, L.; Gerli, P.; Ardito, L.; Petruzzelli, A.M. Smart city governance from an innovation management perspective: Theoretical framing, review of current practices, and future research agenda. *Technovation* **2023**, *123*, 102717. [CrossRef]
17. Ngarambe, J.; Yun, G.Y.; Santamouris, M. The use of artificial intelligence (AI) methods in the prediction of thermal comfort in buildings: Energy implications of AI-based thermal comfort controls. *Energy Build.* **2020**, *211*, 109807. [CrossRef]
18. López-Pérez, L.; Flores-Prieto, J.; Ríos-Rojas, C. Comfort temperature prediction according to an adaptive approach for educational buildings in tropical climate using artificial neural networks. *Energy Build.* **2021**, *251*, 111328. [CrossRef]
19. Zhai, D.; Soh, Y.C. Balancing indoor thermal comfort and energy consumption of ACMV systems via sparse swarm algorithms in optimizations. *Energy Build.* **2017**, *149*, 1–15. [CrossRef]
20. Calama-González, C.M.; Symonds, P.; León-Rodríguez, Á.L.; Suárez, R. Optimal retrofit solutions considering thermal comfort and intervention costs for the Mediterranean social housing stock. *Energy Build.* **2022**, *259*, 111915. [CrossRef]
21. Rossi, F.; Cardinali, M.; Gambelli, A.M.; Filipponi, M.; Castellani, B.; Nicolini, A. Outdoor thermal comfort improvements due to innovative solar awning solutions: An experimental campaign. *Energy Build.* **2020**, *225*, 110341. [CrossRef]
22. Sayad, B.; Alkama, D.; Ahmad, H.; Baili, J.; Aljahdaly, N.H.; Menni, Y. Nature-based solutions to improve the summer thermal comfort outdoors. *Case Stud. Therm. Eng.* **2021**, *28*, 101399. [CrossRef]
23. Chegari, B.; Tabaa, M.; Simeu, E.; Moutaouakkil, F.; Medromi, H. Multi-objective optimization of building energy performance and indoor thermal comfort by combining artificial neural networks and metaheuristic algorithms. *Energy Build.* **2021**, *239*, 110839. [CrossRef]
24. Zhou, Q.; Ooka, R. Implementation of a coupled simulation framework with neural network and Modelica for fast building energy simulation considering non-uniform indoor environment. *Build. Environ.* **2022**, *211*, 108740. [CrossRef]
25. Moon, J.W. Comparative performance analysis of the artificial-intelligence-based thermal control algorithms for the double-skin building. *Appl. Therm. Eng.* **2015**, *91*, 334–344. [CrossRef]
26. Mba, L.; Meukam, P.; Kemajou, A. Application of artificial neural network for predicting hourly indoor air temperature and relative humidity in modern building in humid region. *Energy Build.* **2016**, *121*, 32–42. [CrossRef]
27. Gao, G.; Li, J.; Wen, Y. DeepComfort: Energy-Efficient Thermal Comfort Control in Buildings Via Reinforcement Learning. *IEEE Internet Things J.* **2020**, *7*, 8472–8484. [CrossRef]
28. Chaudhuri, T.; Soh, Y.C.; Li, H.; Xie, L. A feedforward neural network based indoor-climate control framework for thermal comfort and energy saving in buildings. *Appl. Energy* **2019**, *248*, 44–53. [CrossRef]
29. Moon, J.W.; Jung, S.K. Development of a thermal control algorithm using artificial neural network models for improved thermal comfort and energy efficiency in accommodation buildings. *Appl. Therm. Eng.* **2016**, *103*, 1135–1144. [CrossRef]
30. Yu, W.; Li, B.; Jia, H.; Zhang, M.; Wang, D. Application of multi-objective genetic algorithm to optimize energy efficiency and thermal comfort in building design. *Energy Build.* **2015**, *88*, 135–143. [CrossRef]
31. Horikiri, K.; Yao, Y.; Yao, J. Modelling conjugate flow and heat transfer in a ventilated room for indoor thermal comfort assessment. *Build. Environ.* **2014**, *77*, 135–147. [CrossRef]
32. Wang, M.; Li, P.; Liu, W. Generic mathematical formulation of the total heat transfer coefficients between heated radiant floor surfaces and rooms. *Build. Environ.* **2022**, *211*, 108701. [CrossRef]
33. Hu, H.; Wang, H.; Zou, Z.; Zhu, J. Investigation of inter-zonal heat transfer in large space buildings based on similarity: Comparison of two stratified air-conditioning systems. *Energy Build.* **2022**, *254*, 111602. [CrossRef]
34. Aghamolaei, R.; Fallahpour, M.; Mirzaei, P.A. Tempo-spatial thermal comfort analysis of urban heat island with coupling of CFD and building energy simulation. *Energy Build.* **2021**, *251*, 111317. [CrossRef]
35. Florez, F.; Cordoba, P.F.D.; Tost, G.O. Issues regarding the implementation of sliding controls for thermal regulation. In Proceedings of the 4th IEEE Colombian Conference on Automatic Control: Automatic Control as Key Support of Industrial Productivity, CCAC 2019-Proceedings, Medellin, Colombia, 15–18 October 2019. [CrossRef]
36. Florez, F.; Higón, J.; Conejero, J.A.; Córdoba, P.F.D. Modeling and Experimental verification of thermal properties of Thermo Sköld coating solutions. *Mathematics* **2019**, *7*, 503. [CrossRef]
37. Florez, F.; de Córdoba, P.F.; Higón, J.L.; Olivar, G.; Taborda, J. Modeling, simulation, and temperature control of a thermal zone with sliding modes strategy. *Mathematics* **2019**, *7*, 503. [CrossRef]
38. Florez, F.; de Cordoba, P.F.; Taborda, J.; Polo, M.; Castro-Palacio, J.C.; Pérez-Quiles, M.J. Sliding modes control for heat transfer in geodesic domes. *Mathematics* **2020**, *8*, 902. [CrossRef]
39. Florez, F.; Fernández-De-córdoba, P.; Taborda, J.; Castro-Palacio, J.C.; Higón-Calvet, J.L.; Pérez-Quiles, M.J. Passive strategies to improve the comfort conditions in a Geodesic dome. *Mathematics* **2021**, *9*, 663. [CrossRef]
40. Belazi, W.; Ouldboukhitine, S.E.; Chateauneuf, A.; Bouchair, A. Thermal modeling of the occupied multi-zone buildings taking into account the uncertainties of occupant behavior. *Case Stud. Therm. Eng.* **2022**, *33*, 101978. [CrossRef]
41. Tian, W.; Sevilla, T.A.; Zuo, W.; Sohn, M.D. Coupling fast fluid dynamics and multizone airflow models in Modelica Buildings library to simulate the dynamics of HVAC systems. *Build. Environ.* **2017**, *122*, 269–286. [CrossRef]

42. Matyi, M.A.; Cioaba, S.M.; Banich, M.T.; Spielberg, J.M. Identifying brain regions supporting amygdalar functionality: Application of a novel graph theory technique. *NeuroImage* **2021**, *244*, 118614. [CrossRef] [PubMed]
43. Garnier, A.; Eynard, J.; Caussanel, M.; Grieu, S. Predictive Control of Multizone HVAC Systems in Non-residential Buildings. *Ifac Proc. Vol.* **2014**, *47*, 12080–12085. [CrossRef]
44. Brualdi, R.; Cvetkovic, D. *A Combinatorial Apporach to Matrix Theory and Its Applications*; Chapman and Hall/CRC: Boca Raton, FL, USA, 2009.
45. Trevisan, L. *Combinatorial Optimization: Exact and Approximate Algorithms*; Standford University: Standford, CA, USA, 2011.
46. Amin, U.; Hossain, M.J.; Fernandez, E. Optimal price based control of HVAC systems in multizone office buildings for demand response. *J. Clean. Prod.* **2020**, *270*, 122059. [CrossRef]
47. Fei, W.; Ma, Q.; Soga, K.; Narsilio, G.A. A graph-theory based directed network feature for thermal anisotropy. *Int. J. Heat Mass Transf.* **2022**, *194*, 122987. [CrossRef]
48. Eguia-Oller, P.; Martínez-Mariño, S.; Granada-Álvarez, E.; Febrero-Garrido, L. Empirical validation of a multizone building model coupled with an air flow network under complex realistic situations. *Energy Build.* **2021**, *249*, 111197. [CrossRef]
49. Lin, Y.; Middelkoop, T.; Barooah, P. Identification of control-oriented thermal models of rooms in multi-room buildings. In Proceedings of the 2012 IEEE 51st Annual Conference on Decision and Control (CDC), Maui, HI, USA, 10–13 December 2012; pp. 1–27.
50. AutoCAD Software | Get Prices & Buy Official AutoCAD 2023 | Autodesk. Available online: https://www.autodesk.com.sg/products/autocad-lt/overview?term=1-YEAR&tab=subscription (accessed on 27 January 2023).
51. Ogata, K.; Bermúdez, E.P.; Matía, F.; Pearson, E.; Hall, P.; Dorf, R.C.; Pearson, R.H.B. *Ingeniería de Control Moderna*; Pearson Education: London, UK, 2010; p. 909.
52. Goyal, S.; Barooah, P. A method for model-reduction of non-linear thermal dynamics of multi-zone buildings. *Energy Build.* **2012**, *47*, 332–340. [CrossRef]
53. Kossak, B.; Stadler, M. Adaptive thermal zone modeling including the storage mass of the building zone. *Energy Build.* **2015**, *109*, 407–417. [CrossRef]
54. Atam, E. Decentralized thermal modeling of multi-zone buildings for control applications and investigation of submodeling error propagation. *Energy Build.* **2016**, *126*, 384–395. [CrossRef]
55. Royer, S.; Thil, S.; Talbert, T.; Polit, M. A procedure for modeling buildings and their thermal zones using co-simulation and system identification. *Energy Build.* **2014**, *78*, 231–237. [CrossRef]
56. Coutinho, C.P.; Baptista, A.J.; Dias, J. Reduced scale models based on similitude theory: A review up to 2015. *Eng. Struct.* **2016**. *119*, 81–94. [CrossRef]
57. Liu, P.C.; Lin, H.T.; Chou, J.H. Evaluation of buoyancy-driven ventilation in atrium buildings using computational fluid dynamics and reduced-scale air model. *Build. Environ.* **2009**, *44*, 1970–1979. [CrossRef]
58. Walker, C.; Tan, G.; Glicksman, L. Reduced-scale building model and numerical investigations to buoyancy-driven natural ventilation. *Energy Build.* **2011**, *43*, 2404–2413. [CrossRef]
59. Guo, P.; Wang, S.; Xu, B.; Meng, Q.; Wang, Y. Reduced-scale experimental model and numerical investigations to buoyance-driven natural ventilation in a large space building. *Build. Environ.* **2018**, *145*, 24–32. [CrossRef]
60. Rizzo, F.; Ricciardelli, F.; Maddaloni, G.; Bonati, A.; Occhiuzzi, A. Experimental error analysis of dynamic properties for a reduced-scale high-rise building model and implications on full-scale behaviour. *J. Build. Eng.* **2020**, *28*, 101067. [CrossRef]

Disclaimer/Publisher's Note: The statements, opinions and data contained in all publications are solely those of the individual author(s) and contributor(s) and not of MDPI and/or the editor(s). MDPI and/or the editor(s) disclaim responsibility for any injury to people or property resulting from any ideas, methods, instructions or products referred to in the content.